N87-19335

CHAPTER 5: FLARE ENERGETICS

S.T. Wu[1], C. de Jager[2], B. R. Dennis[3], H. S. Hudson[4], G. M. Simnett[5], K. T. Strong[6], R. D. Bentley[7], P. L. Bornmann[8], M. E. Bruner[6], P. J. Cargill[9], C. J. Crannell[3], J. G. Doyle[10], C. L. Hyder[11], R. A. Kopp[12], J. R. Lemen[7], S. F. Martin[13], R. Pallavicini[14], G. Peres[15], S. Serio[15], J. Sylwester[16], and N. J. Veck[17]

[1]University of Alabama, Huntsville, Alabama
[2]Space Research Laboratory, Utrecht, The Netherlands
[3]NASA Goddard Space Flight Center, Greenbelt, Maryland
[4]University of California at San Diego, California
[5]University of Birmingham, England
[6]Lockheed Palo Alto Research Laboratory, Palo Alto, California
[7]Mullard Space Science Laboratory, England
[8]Joint Institute for Laboratory Astrophysics, Boulder, Colorado
[9]National Center for Atmospheric Research, Boulder, Colorado
[10]Armagh Observatory, Northern Ireland
[11]High Altitude Observatory, Boulder, Colorado
[12]Los Alamos Scientific Laboratory, Los Alamos, New Mexico
[13]California Institute of Technology, Pasadena, California
[14]Observatorio Astrofisico di Arcetri, Firenze, Italy
[15]Observatorio Astronomico di Palermo, Palermo, Italy
[16]Instytut Astronomiczny, Wroclaw, Poland
[17]Marconi Research Center, Chelmsford, England

ABSTRACT

In this investigation of flare energetics, we have sought to establish a comprehensive and self-consistent picture of the sources and transport of energy within a flare. To achieve this goal, we chose five flares in 1980 that were well observed with instruments on the Solar Maximum Mission, and with other space-borne and ground-based instruments. The events were chosen to represent various types of flares. Details of the observations available for them and the corresponding physical parameters derived from these data are presented. The flares were studied from two perspectives, the impulsive and gradual phases, and then the results were compared to obtain the overall picture of the energetics of these flares. We also discuss the role that modeling can play in estimating the total energy of a flare when the observationally determined parameters are used as the input to a numerical model. Finally, a critique of our current understanding of flare energetics and the methods used to determine various energetics terms is outlined, and possible future directions of research in this area are suggested.

5.1 INTRODUCTION

S.T. Wu and C.J. Crannell

5.1.1 Objectives of Study

Understanding the flow of energy in a solar flare represents a good test of our knowledge of flare physics. Accordingly, this team has sought to identify the major sources and sinks of flare energy, together with the mechanisms by which the energy flows from one form to another. By doing this quantitatively we have sought to establish a comprehensive and self-consistent picture of the sources and transport of energy within a flare. To undertake this study, we use theoretical modeling and observations obtained with the Solar Maximum Mission (SMM), other satellites, and groundbased facilities. The perspective from which these objectives were pursued and the scope of the flare observations available for this effort are described in the following subsections.

5.1.2 Perspective-Skylab to SMM

Skylab Solar Workshop II (Sturrock, 1980) focused on observations of solar flares obtained with the first full-scale, manned, astronomical observatory in space. This observatory carried instruments covering the wavelength range from 2 to 7000Awhich encompasses the soft X-ray, UV, and visible light portions of the electromagnetic spectrum. Photographs of active regions and flares in progress provided unprecedented graphic documentation of the role of magnetic loops and multi-thermal plasmas in the storage and release of flare energy. The data from Skylab added to the results obtained during the preceding solar maximum from Orbiting Solar Observatories and other unmanned satellites, which had charted the dominant role of high-energy radiations in defining solar flare physics. SMM was designed to make coincident observations of as many aspects of solar flares as possible. The emphasis with SMM instrumentation was on comprehensive coverage, and despite unfortunate gaps, particularly in measurements of coronal lines, the observations available for this workshop reflect that emphasis. The observations obtained with SMM benefit, as well, from improvements in sensitivity and temporal resolution, particularly for the highest energy electromagnetic radiation. A major advance achieved with SMM is the capability of imaging X-rays with energies up to 30 keV. The availability of broad observational coverage guided the approach adopted by this team, which attempted to establish a global view of flare energetics. The key questions addressed from this perspective are presented in the following subsection.

5.1.3 Key Questions

A wide variety of electromagnetic and particle radiations are observed in solar flares. Although there are many questions about the mechanisms whereby these radiations are produced, there is a general consensus that conversion of magnetic energy provides the fundamental energy source. The location of the energy source itself is not known. To investigate the associated energy sources and their transport processes, we have classified the flare phases by their time structures as being either impulsive or gradual. The impulsive phase is usually characterized by hard X-ray and microwave spikes with timescales in the range from fractions of a second to a few tens of seconds. The gradual phase, on the other hand, has time-scales on the order of minutes or even hours. The work reported in this chapter addresses the following key questions about these two phases:

- How do we characterize the impulsive phase?
- Do all flares have an impulsive phase?
- What is the total energy content of the flare in the impulsive phase?
- What is the relative importance of the thermal and the non-thermal components of the impulsive phase of the flare?
- How does the energy in the sources associated with the gradual phase emissions compare with that attributable to impulsive phase energy sources?
- What are the dominant cooling mechanisms at different stages of the gradual phase?
- Do all the post-flare loops need continual energy input?
- Are there extended, late, flare-associated sources in the corona?

5.1.4 Approach Adopted for Study

The distribution of the total flare energy among various reservoirs and active phenomena is illustrated in Figure 5.1.1. In this diagram, we sketch, as a function of time throughout the pre-flare, impulsive, and gradual phases, the integral energy content in the following forms:

- radiant energy
- thermal plasma energy
- gravitational potential energy
- kinetic energy of accelerated particles
- kinetic energy in plasma flows and random motions.

We used this schematic representation to compare the magnitudes of different manifestations of flare energy. The underlying assumption is that the energy flows from the magnetic reservoir, which is continuously being fed by large-scale flows, so that Figure 5.1.1 represents a sudden decrease in the magnetic free energy. Figure 5.1.1 is highly nonlinear since it represents cumulative contributions of terms with very different magnitudes. It is mainly helpful for qualitatively visualizing the processes involved in the energetics analysis.

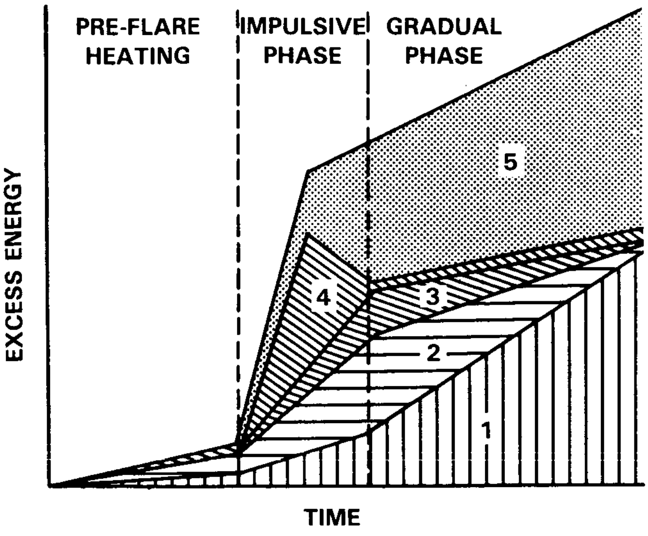

Figure 5.1.1 This diagram shows conceptually how the energy of a flare is partitioned into its various forms as a function of time. Plotted in the graph are the excess energies above the active region thermal energy, which is assumed to remain constant throughout the flare. The total energy of the system, including the magnetic free energy, is very large compared to the flare energy. During pre-flare heating, there is an increase in the radiant energy (1), the thermal energy of the plasma (2), and the gravitational potential energy (3) as material is carried into the coronal loops. During the impulsive phase, these quantities rise more rapidly with a significant increase in the energy in non-thermal particles (4) and mechanical energy (5). During the gradual phase, there may be some continued heating by non-thermal particles but eventually all the energy produced by the flare is left in the form of energy lost by radiation (1) or in the coronal transient (5).

Similarly, Figure 5.1.2 has been used to illustrate the flow and transport of flare energy. In this scheme, we again show the five energy sources or sinks shown in Figure 5.1.1 but also include the following energetically significant interconnecting terms:

- direct heating
- conductive heating
- radiative heating
- heating by particles
- radiative loss
- evaporation
- anti-evaporation ("coronal rain")
- shock and turbulent heating
- mechanical energy losses
- shock and turbulent acceleration of particles

- direct acceleration of particles
- direct mass acceleration

Any of these terms could be broken down into finer detail: for example, the heating due to radiation represents, in general terms, the entire field of radiative transfer.

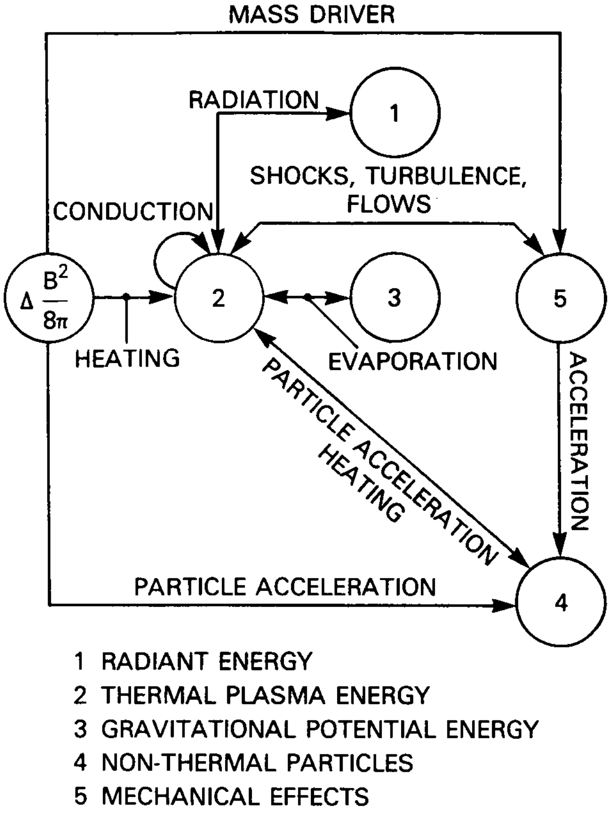

Figure 5.1.2 This diagram illustrates how energy is transferred between the various sinks or reservoirs (circles). The energy sinks are (1) radiation, (2) thermal plasma, (3) gravitational potential energy, (4) nonthermal particles, and (5) mechanical effects. The interconnecting lines indicate the possible mechanisms and directions of energy transfer between the sinks.

The energy content of various flare components can be estimated from the observable emissions associated with the interactions of these constituents with each other and with the ambient solar medium. In most cases, such estimates are model dependent, with the attendant disadvantage that the energy determinations are not unique. On the other hand, any systematic differences between the results obtained for the whole flare energetics with different models provide a means of discriminating among them.

5.1.5 Data Characterization

The question of data presentation is an inevitable compromise between completeness and compactness. The approach that we follow in this chapter is that of presenting the data in parametric form, in which a theoretical relation involving a relatively small number of variables is used to represent the observations. Although the names of the parameters usually correspond to physically meaningful quantities such as temperature, density, or volume, the parameters themselves may not be accurate measures of these quantities. A temperature, for example, may accurately represent the slope of an observed spectrum over a limited energy range, even though the energy distribution of the source particles is non-Maxwellian.

For line profiles from the Ultraviolet Spectrometer and Polarimeter (UVSP) and for the Bent Crystal Spectrometer (BCS) and P78-1 emission line observations, we have used a Gaussian parameterization, stating the amplitude and central wavelength as functions of time throughout the period of the observations.

The Hard X-Ray Burst Spectrometer (HXRBS) and the Hard X-ray Imaging Spectrometer (HXIS), which are based on scintillation counters and proportional counters, respectively, are inherently broad-band instruments with spectral resolutions of a few points per decade of energy. Some HXRBS spectra are well represented by a thermal bremsstrahlung model, others by a power law, and some by both parametric forms. In either case, the practice followed has been to perform a convolution of the X-ray spectrum computed for an assumed electron energy distribution with the instrument response function and to adjust the parameters of the assumed distribution for best fit of the computed X-ray spectrum to the observations.

Ratios among the HXIS bands are a measure of the average slope of the spectrum, which, in turn, can be represented by a temperature parameter. Some measure of the consistency of this description can be found in the comparison of temperature parameters derived from different ratios.

The Flat Crystal Spectrometer (FCS) and BCS measure line spectra for which the thermal or power-law representations are inappropriate. Most FCS observations are made in a raster pattern in the seven home-position lines. These data are described for purposes of this chapter by a differential emission measure distribution computed by following the methods of Sylwester *et al.* (1980). This representation approximately reproduces the observed intensities and derives some compactness from the sum over the raster, but must still be presented as a curve for each observation. Further details are given in Section 5.3.

We alert our readers to the use of parameterization throughout the remainder of this chapter and urge them to draw careful distinctions between parameters used to characterize the data and the interpretation of the data in terms of physical quantities. The term 'temperature' should be understood to mean temperature parameter when we are referring to the results of a thermal fit to an observed spectrum. In the power law representation of the spectrum, the parameters are the hardness index and the photon flux at a given energy. Electron densities derived from line ratios in the UVSP or P78-1 observations are referred to as 'derived electron densities'. Similarly, temperatures derived from either BCS or P78-1 line ratios should be understood to be 'derived temperatures', even when this is not explicitly stated.

5.1.6 Observations and Their Interpretation

Details of the observations made with the different SMM instruments are given in the discussion of each of the flares studied. Here we summarize the types of observations that are available and their interpretations.

Observations of gamma-ray emission obtained with the Gamma Ray Spectrometer (GRS) were used to estimate the energy content of the energetic protons and ions ($>$ 10 MeV) participating in selected flares. The observed fluxes and upper limits were used with the model of Ramaty (1982) to obtain scaled energy estimates and upper limits. Uncertainties in these values are dominated by the uncertainty in the choice of the appropriate spectral form. The observations constrain the numbers of protons and ions only for energies above 10 MeV.

Hard X-ray observations obtained with HXRBS and microwave observations obtained with the radio telescopes at Bern, Toyokawa, Nobeyama, and Nagoya, and with the Radio Solar Telescope Network (RSTN) were used to estimate the flare energy in the form of energetic electrons. Two models (a non-thermal, thick-target model and a thermal model) were used to obtain two different estimates of the electron energy associated with selected flares. In the non-thermal model, it is assumed that the hard X-rays are electron-ion bremsstrahlung produced as an electron beam arrives at the footpoints of a magnetic loop. Standard thick-target equations were used (Brown 1971, Hoyng *et al.*, 1976, Lin and Hudson 1976) with a power-law spectral fit and a cut-off of 25 keV.

In the thermal model, it is assumed that the hard X-ray emission and the optically-thick microwave emission originate in a common hot plasma with the temperature, density, and source area consistent with the coincident observations. The effective temperature and emission measure are determined from a spectral fit to the hard X-ray observations, and the source area is determined from the microwave observations.

The energy components of the thermal plasma were estimated from combined data sets obtained with HXIS, BCS, and FCS. The HXIS images with 8 arcsec (FWHM) resolution were used to provide estimates of the flare area from which flare volumes were derived by assuming simple geometric models. The FCS also provides imaging but at a relatively lower resolution (14 arcsec FWHM). Thus, the FCS images were used mainly in a qualitative fashion to compare with the HXIS images, especially at lower temperatures (10^6 to 5×10^6K).

All three instruments are capable of providing isothermal model estimates of the temperature and emission measure from which it is possible to derive the thermal energy. However, the preferred technique for deriving estimates of the thermal energy was to combine the observed fluxes from HXIS and BCS (and from FCS in at least one flare) in a multi-thermal model for the emission measure. The thermal energy of plasmas at temperatures above 10^7K (2×10^6K when FCS data were included) could then be obtained by using the volume derived from the HXIS measurement of the flare area and assuming a filling factor of unity.

The BCS is also capable of measuring two non-thermal energy components: the energy of plasma flows and the energy in the random motions of the turbulent plasma. During the rising portion of the soft X-ray flare, blue-ward broadening of the soft X-ray lines has been observed with BCS and interpreted as Doppler-shifted radiation from chromospherically evaporated plasma. The measured velocities of the upflowing plasma are typically 150 to 250 km s^{-1}, from which the kinetic energy was estimated. The energy in the random motion of the turbulent plasma is estimated from the symmetric line broadening of the soft X-ray spectra in excess of that expected from a thermal source with equal ionic and electron temperatures.

Information derivable from UVSP observations depends on the observing mode that was used. Most observations are relevant to the transition zone, although some chromospheric and coronal lines were also observed. Some modes are velocity sensitive, whereas others yield density-sensitive line ratios.

5.1.7 Flares Chosen for Study

We have chosen five flares from the SMM data set which we felt to be representative of different types of solar flares. Appendix 5A summarizes the properties of these flares, which were as follows:

- a flare of moderate strength (GOES class M) from an extended active region producing frequent flares (1980 April 8 at 03:04 UT);
- a large, two-ribbon flare which produced interplanetary protons at energies of >40 MeV (1980 May 21 at 20:53 UT);
- a moderate limb flare accompanied by a coronal transient (1980 June 29 at 18:03 and 18:22 UT);
- a compact double flare (1980 August 31 at 12:48 and 12:52 UT);
- a major double flare (1980 November 5 at 22:26 and 22:33 UT).

These flares will be familiar to readers of other chapters of this volume. We included double flares in an effort to study the effect of various initial conditions. All of the chosen flares had full SMM instrument coverage with the exception of that on June 29, for which the main flare site was not observed with UVSP; in addition there are no Coronograph/ Polarimeter (C/P) observations except for the June 29 event. Full details and bibliographies of published material on these flares appear in Appendix 5A; we summarize their properties in Table 5.1.1.

Table 5.1.1 Flares Chosen for Detailed Study

Date in 1980	Onset time (UT)	Location	Optical class	GOES class	Peak rate >28 keV (counts s^{-1})	Peak microwave flux at 8.8 GHz (s.f.u.)
Apr 8	03:04	N12 W13	1B	M4	3800	200
May 21	20:53	S14 W15	2B	X1	14300	1200
Jun 29	18:03	S29 W90	limb	M1	441	
	18:22	S29 W90	limb	M4	3177	74
Aug 31	12:48	N12 E28	−B	C6	7360	556
	12:52	N12 E28	−B	M2	3673	
Nov 5	22:26	N11 E07	1B	M1	3151	
	22:33	N11 E07	1B	M4	12730	3100

These all appear to be type B flares according to the classification scheme proposed originally by Tanaka (1983) and developed by Ohki *et al.* (1983) and Tsuneta (1983). None of the events we selected for detailed analysis is a type A or a type C flare. Type A flares are low-altitude, compact (< 10 arc sec) flares with very steep hard X-ray spectra and have been interpreted as purely thermal flares with temperatures of 3×10^7 to 5×10^7 K (Tsuneta *et al.*, 1984a). Type C flares have virturally no impulsive phase, and the hard X-rays and microwaves appear to come, in at least one case, from altitudes of 5×10^4 km, near the top of a huge coronal loop (Tsuneta *et al.*, 1984b). Cliver *et al.* (1984) have suggested that many flares that show similar characteristics to type C flares may be preceded some tens of minutes earlier by an apparently normal impulsive flare, presumably of type B. This classification scheme is described in more detail in Chapter 3 of this Workshop Report.

The concentration on type B flares was dictated by SMM observations, since the best observed flares were of this type. A further limitation of this work is the absence of a solar flare showing gamma-ray line emission. This again reflects the SMM data set in which there are no gamma-ray flares observed with the imaging instruments.

The growth of active-region magnetic energy has been estimated by using an MHD model given by Wu *et al.* (1983). This model is used to estimate the energy build-up during the pre-flare state on the basis of photospheric shearing motions. Wu *et al.* found that, in this model, the majority of the energy storage is magnetic; other forms (kinetic, potential, or thermal) are negligibly small in the pre-flare state. The physical basis of this MHD model is that observed shear motion at the photosphere is the result of motion of the magnetic loop footpoints. This movement causes the magnetic field to twist and hence magnetic energy to be stored. Because the movement is so slow (~ 100 m s^{-1}), the quasi-equilibrium state is always maintained so that the other energy modes do not increase as significantly as the magnetic energy.

5.1.8 Synopsis

In this investigation of flare energetics, observations characterizing the impulsive and gradual phases first were analyzed separately and then the results of the individual analyses were intercompared. Observational and analytic results related to the energetics of the impulsive phases of the events chosen for this study are presented in the following section. In Section 5.3, results obtained for the energetics of the gradual phases are presented. Investigation of the energetics relationships between the impulsive and gradual phases is described and their interpretation in terms of flare models is discussed in Section 5.4. In Section 5.5, an attempt is made to present a synthesis, based on the foregoing results, characterizing the total flare energy. Conclusions based on this work and observational requirements for addressing the remaining questions with instruments to be employed in the future are presented in Section 5.6. Appendix 5A describes the published results and observations of the five flares chosen for detailed study in this chapter. Appendix 5B contains a review of the observational characteristics of the impulsive phase of flares in general.

5.2 ENERGETICS OF THE IMPULSIVE PHASE

C. de Jager, M.E. Bruner, C.J. Crannell, B.R. Dennis, J.R. Lemen, and S.F. Martin

5.2.1 Introduction

In this section we concentrate on the impulsive phase, with particular emphasis on the energy content of the different components of the prime flares chosen for study (see Appendix 5A). From an energetics point of view, we are concerned primarily with high-energy electrons and protons and with plasma at temperatures above 10^4 K. The different forms of energy include the kinetic energy of fast particles, and the thermal, convective, and turbulent energies of hot plasma. Our approach is in contrast to that used by Canfield *et al.* (1980), who presented estimates of the total radiant energy in different wavelength ranges. We have also measured the radiant energy in soft and hard X-rays, and in Hα for one flare, and the results are discussed in Section 5.4. We find that the energy radiated during the impulsive phase is negligible compared with the other components of the total flare energy. A more detailed discussion is given of the radiant energy as determined from the new Hα observations because they give a better estimate of the Hα radiant energy from one flare than that obtained previously (see Section 5.2.3.5).

To estimate the energies in the different flare components, it is necessary to make various assumptions about the physical conditions in the flares. Unfortunately, these cannot be determined umambiguously from the available observations. In particular, the thermal or nonthermal nature of the hard X-ray source is still unresolved, in spite of considerable evidence favoring the existence of beams of fast electrons. The spectrum of electrons below 20 keV, where most of the total energy may reside, is subject to large uncertainties. Also, only upper limits can be placed on the energy in protons above a few MeV from the gamma ray observations of the flares considered here. There is no information at all on the possible existence of protons at 10 keV to 1 MeV, which have been postulated to be an important component during the impulsive phase (Simnett 1984).

For the thermal plasma emitting soft X-rays, the filling factor and density distribution are also largely unknown. In addition, the available observations for the prime flares studied here do not provide information on the energy of plasma with temperatures below 10^6K.

As a result of these gaps in our knowledge, the energy of some potentially important components of flares cannot be estimated at all, and order-of-magnitude uncertainties exist in many of the estimates that can be made. Nevertheless, it is important in furthering our understanding of the flare processes to make these estimates as accurately as possible. Not only do they provide valuable limits on the total flare energy, but also, and possibly more importantly, they suggest how the energy is distributed among the components as a function of time during the various stages of the flare. The ability to determine these temporal variations in the distribution of the flare energy is improved markedly with the observations available for this study. Time resolutions as short as 0.1 s for the hard X-ray spectral observations and a few seconds for the X-ray imaging and soft X-ray spectral observations allow the flare energies to be determined on timescales an order of magnitude shorter than previously possible.

We begin Section 5.2.2 with a working definition of the impulsive phase and a brief review of the observations from which we obtained our energy estimates. We have concentrated on, but have not restricted ourselves to, the flares described in Appendix 5A that were selected by this team for detailed analysis. Estimates of the energies involved in energetic electrons, protons, and ions, chromospheric evaporation, and the thermal plasma at temperatures above 10^7K are given in Section 5.2.3. A more detailed description of the analysis done for the 1980 April 8 flare is given in Section 5.2.4. Finally, in Section 5.2.5 the main results are summarized and the relation between soft and hard X-ray sources is discussed.

5.2.2 The Characteristics of the Impulsive Phase

A review of the observational characteristics of the impulsive phase of flares is given in Appendix 5B, and a more extensive discussion is contained in Chapter 2 of this report. The most important characteristic of this phase is the impulsive release of energy on timescales of less than or about 10 s. This is evidenced by the plots of the intensity of the hard X-ray flux versus time that are shown in Figures 5A.2, 4, 7, 10, and 12. The hard X-ray spectral observations allow us to estimate the energy in fast electrons as discussed in Section 5.2.3.1. The soft X-ray flux shown as a function of time in the same figures rises continuously during the time that the hard X-rays are observed. Measurement of the line and continuum emissions allows us to estimate the energy of the hot plasma during this period (Sections 5.2.3.3 and 5.2.3.4).

5.2.3 The Determination of Component Energies

In this section we describe the methods that we used to determine the energies of several of the energetically most important flare components during the impulsive phase. We considered the following flare components: (a) impulsive energetic electrons that produce hard X-rays, (b) energetic protons and ions that produce gamma rays, and (c) thermal plasma that produces soft X-rays.

Two different estimates of the energy in the fast electrons were obtained from the hard X-ray observations; the first was obtained under the assumption that the X-rays were produced in non-thermal, thick-target interactions, and the second was obtained under the assumption that the hard X-rays and microwaves were produced in the same thermal source at a temperature in excess of 10^8K. The energy in the soft X-ray-emitting plasma includes the kinetic energies of the convective and turbulent plasma motions in addition to the thermal energy. The radiative and conductive energy losses from this thermal plasma were also considered but were generally negligible during the impulsive phase, as was the gravitational potential energy of the upflowing plasma.

5.2.3.1 The Energy in Impulsive Energetic Electrons

It is almost universally accepted that solar flare hard X-rays are electron-ion bremsstrahlung. Since the bremsstrahlung cross-section as a function of energy is well known, it is possible to determine the instantaneous energy spectrum of the emitting electrons from the measured X-ray spectrum. Unfortunately, the interpretation of this result depends on the temperature and density of the plasma in which the electrons are interacting. Three basic models have been proposed for the production of the hard X-rays: models based on thick- and thin-target interactions and a thermal model (Brown 1971, Lin and Hudson 1976; Tucker 1975; Crannell *et al.*, 1978). It is necessary to know, in any particular flare, which model (or combination of models) is correct, since the determination of the electron spectrum from the observed X-ray spectrum depends on the model assumed. More importantly, the correct model must be known to determine the role of the fast electrons in the overall flare energetics and ultimately to determine the fundamental energy release mechanism or mechanisms of the flare.

Recent observations have shown that the thick-target model is most likely to be the correct one, at least during the *early* part of the impulsive phase of *some* flares and for *some* fraction of the total hard X-ray flux. The arguments supporting this statement are presented in Appendix 5B. However, the subject is still controversial, and there is a strong possibility that a large fraction of the hard X-ray flux comes from a thermal source. This controversy is touched on in Appendix 5B, and a more detailed discussion can be found in Chapter 2 of this report.

From a spectral point of view, the hard X-ray observations used to make the energy estimates are consistent with either a thick-target or a thermal model. The X-ray spectrum can often be represented within the uncertainties of the data by either a power law or the exponential function expected for an isothermal source. Sometimes the thermal bremsstrahlung function fits the observations better on the rise and at the peak of impulsive bursts, whereas a power law fits better on the decline and in the valley between adjacent bursts (Crannell *et al.*, 1978; Dennis, *et al.*, 1981; Kiplinger *et al.*, 1983a). However, a non-thermal source can produce an exponential spectrum, and a multi-temperature thermal source can generate a power-law spectrum (Brown 1974). In estimating the energy in fast electrons, therefore, we have chosen to make the calculations both for a thick-target model by assuming a power-law spectrum and for a single-temperature thermal model. The true model is probably some hybrid of the two, but we are unable to determine the proportions of the thermal and non-thermal components from the available observations.

(i) *Non-thermal Model.* The X-ray spectra of the impulsive bursts have been determined from HXIS and HXRBS observations by using techniques described by Batchelor (1984). By assuming thick-target interactions, we can determine the energy and the number of energetic electrons involved in the bombardment of the lower corona and the chromosphere from these X-ray spectra.

For calculating the energy in fast electrons, one usually assumes that the incident X-ray spectrum is a power law of the form

$$I_x(\epsilon) = \alpha\, \epsilon^{-\gamma} \text{ photons cm}^{-2}\text{ s}^{-1}\text{ keV}^{-1}, \qquad (5.2.1)$$

where $I_x(\epsilon)$ is the differential flux of photons with energy ϵ in keV, and α and γ are parameters determined from least-squares fits to the spectral data. The standard thick-target-model equations are used to relate the measured X-ray spectrum to the spectrum of the electrons producing the X-rays (Brown 1971; Hoyng *et al.*, 1976; Lin and Hudson 1976). The electron spectrum that results in a power-law X-ray spectrum is also a power law, of the form

$$I_e(E) = \beta\, E^{-\delta} \text{ electrons s}^{-1}\text{ keV}^{-1}, \qquad (5.2.2)$$

where $I_e(E)$ is the differential flux of electrons with energy E that enter the thick target. The parameters β and δ are related to α and γ by the following equations:

$$\beta = 3 \times 10^{33}\, \alpha\, \gamma(\gamma - 1)^2 \\ b(\gamma - 1/2,\ 1/2), \qquad (5.2.3)$$

$$\delta = \gamma + 1, \qquad (5.2.4)$$

where $b(\gamma - 1/2, 1/2)$ is the beta function.

The total energy in electrons that enter a thick target during a flare is obtained from the equation

$$W(>E_0) = \int\int_{E_0}^{\infty} \beta\, E^{-\delta+1}\, dE\, dt = \\ \int \beta E_0^{-\delta+2}\, (\delta - 2)^{-1}\, dt \qquad (5.2.5)$$

In this expression, the lower energy cut-off, E_0, must be imposed on the electron spectrum to ensure that W remains finite, but it is very difficult to determine the correct value of E_0 from the observations. This difficulty introduces the largest uncertainty in the estimate of W. A cut-off in the electron spectrum at E_0 would appear as a flattening of the X-ray spectrum at X-ray energies below E_0. The X-ray spectrum cannot get significantly flatter than ϵ^{-2}, however, as a result of the Bethe-Heitler formula for the bremsstrahlung cross section, regardless of the shape of the electron spectrum. Such a flattening at low energies is sometimes observed in the X-ray spectrum at the time of impulsive peaks in the flux, although it can be masked by the soft X-ray flux from the $\sim 20 \times 10^6$ K plasma. As a suitable approximation, $E_o = 25$ keV has been taken for the calculation of the values of W given in Tables 5.2.1 and 5.2.2.

(ii) ***Thermal Model.*** An alternative model for the production of the hard X-rays is one in which the source is thermal and the electron spectrum can be represented with a single effective temperature. The X-ray continuum spectrum is then of the form expected from an electron population with a Maxwellian velocity distribution, i.e.,

$$I_x(\epsilon) = 1.08 \times 10^{-42}\, Y\, \epsilon^{-1}\, T^{-0.5}\, G(\epsilon,T) \exp(-\epsilon/kT) \text{ photons cm}^{-2}\text{ s}^{-1}\text{ keV}^{-1}, \qquad (5.2.6)$$

where Y is the thermal emission measure (in cm^{-3}), T is the effective temperature of the source (in degrees K), $G(\epsilon,T)$ is the "total effective Gaunt factor" as a function of ϵ and T as given by Mewe and Gronenschild (1981) and Matteson (1971), and k is the Boltzmann constant. The parameters Y and T are selected to give a least-squares fit to the HXRBS spectral data (Batchelor 1984).

The thermal energy in the isothermal plasma emitting the hard X-rays is given by the relation

$$E_{th} = 4.14 \times 10^{-16}\, Y\, T/n \text{ ergs} \qquad (5.2.7)$$

where n is the electron density (in cm^{-3}). Since $Y = n^2 V_p$, where V_p is the volume of the plasma (in cm^3), the thermal energy can be rewritten as

$$E_{th} = 4.14 \times 10^{-16}\, Y^{1/2}\, V_p^{1/2}\, T \text{ ergs}. \qquad (5.2.8)$$

Thus, either the density or the volume of the source must be known before E_{th} can be determined.

An estimate of the source volume can be obtained from the microwave data with the additional assumptions that the observed optically-thick microwave emission originates with the hard X-rays in a common, thermal source. In such a model, the frequency-dependent flux $I_\mu(f)$ in the optically-thick portion of the microwave spectrum is related to the projected source area A_μ (in cm^2) by the expression

$$I_\mu(f) = 1.38 \times 10^{-26}\, f^2\, A_\mu\, T, \qquad (5.2.9)$$

where $I_\mu(f)$ is measured in solar flux units (1 sfu = 10^{-22} W m^{-2} Hz^{-1}) and f is the observing frequency in GHz (Crannell *et al.*, 1978). This relation provides a means for determining the area of the source region through the use of the temperature determined from the hard X-ray observations and the microwave flux measured at fixed frequencies in the optically thick portion of the spectrum.

The volume of the source (V_p) can be estimated from A_μ by

$$V_p = A_\mu^{3/2}, \qquad (5.2.10)$$

so that the expression for the thermal energy can be rewritten as

$$E_{th} = 4.14 \times 10^{-16}\, Y^{1/2}\, A_\mu^{3/4}\, T \text{ ergs}. \qquad (5.2.11)$$

Similarly, the magnetic field associated with the source region can be inferred from the calculated temperature and the turnover frequency in the microwave spectrum, f_t (in GHz), according to the following simplified relation (Karpen, *et al.*, 1979):

$$B = 1.86 \times 10^4 \left[f_t/(1.66 \times 10^8 + T)\right]^{1.14}. \qquad (5.2.12)$$

The values of the calculated parameters are given in Table 5.2.3.

5.2.3.2 Estimates of the Energy Content of the Energetic Protons and Ions

The three prime flares listed in Table 5.2.4 were observed with GRS at energies above 300 keV. However, none of them produced detectable nuclear line emission above the GRS sensitivity threshold. Therefore, although we have no direct measure of the gamma-ray flux resulting from the interactions of energetic protons and ions, we do have upper limits on this flux for each of the events which produced continuum emission above 300 keV. These upper limits can be used with the model described by Ramaty (1982) to deduce upper limits on the energy content of the energetic protons and ions above a few MeV. The values obtained in this fashion for each of the three flares are presented in Table 5.2.4.

In addition to these upper limits, an estimate of the energy content of the energetic protons and ions can be obtained from the observed continuum emission above 300 keV and an empirically determined scaling factor relating the continuum flux and the nuclear line emission. The values presented in the fourth and fifth columns of Table 5.2.4 are energy estimates obtained with this scaling procedure used in conjunction with the model described by Ramaty (1982), and the same spectral shape as was the upper limits. For two of the three flares, the estimates are significantly less than the corresponding upper limits. For one flare, the estimates are greater than the upper limits, but the difference is not significant.

Realistic uncertainties in the values of the estimates and upper limits are dominated by the uncertainty in the choice of the appropriate spectral form. In Ramaty's model calculations, a Bessel function spectral form is used. Alternative

Table 5.2.1 Flare Parameters Derived from HXIS and HXRBS Data

Date 1980	SXR Peak Time (UT)	Temperature (10^6K)	Emission Measure (10^{48} cm^{-3})	Volume (10^{26} cm^3)	Density (10^{10} cm^{-3})	Thermal Energy, U (10^{29} ergs)	Energy in Electrons W(>25 keV) (10^{29} ergs)
Apr 8	03:07	25.2	13.8	5.9	15	9.4	94
			5.2	62	2.9	19	
Apr 10	09:21:30	23.7	20.3	7.6	16	12	49
Apr 13	04:08	25.5	1.5	1.3	11	1.5	7
			2.3	36	2.5	9.6	
Apr 30	20:25	20.5	6.3	2.9	15	3.6	7
			1.9	28	2.6	6.2	
May 9	07:13:30	23.7	41.3	1.0	64	6.3	23
May 21	21:05	21.3	76	25	17	38	96/110
			27	40	8.2	29	
Jun 13	22:34:20	21.4	5.5	Edge of fine FOV			5
Jun 25	15:54			No HXIS Data			54
Jun 29	02:38	18.5	17	HXIS coarse FOV			49
Jun 29	10:43:15	18.5	28	HXIS coarse FOV			34
Jun 29	18:25:40	20.2	28	HXIS coarse FOV			13-93
Jul 1	16:28:50			Out of HXIS FOV			80
Jul 5	22:44:40	26.7	42	1.0-2.9	65-38	7-12	48
Jul 7	11:52:00	24.4	3.4	2.1	1.3	2.7	6
Jul 12	11:19:15			HXIS coarse FOV			
Jul 12	11:23:20			HXIS coarse FOV			142
Jul 14	08:27:00	18.4	76.5	4.3	42	14	12
Jul 21	03:00:40			No HXIS data			225
Aug 23	21:30	20.6	4.4	2.3	14	2.7	9
			2.8	14	4.5	5.3	
Aug 24	16:12:30	19.2	4.5	Edge of HXIS fine FOV			12
Aug 25	13:05:30	21.4	1.9	Edge of HXIS fine FOV			8
Aug 31	12:49:30	17.5	3.1	3.3	9.7	2.3	3.3
Aug 31	12:52:30	20.5	11.2	0.76	38	2.5	5
Sep 24	07:34:30	21.8	5.5	7	8.8	5.6	<7.5
Nov 5	22:28:17	20	3.1	3.3	9.7	2.6	1.6
Nov 5	22:35:30	25.9	14.2	14	10	15	28
			2.0	34	2.4	8.8	
Nov 6	17:27:30	29.1	2.4	0.32	28	1.1	Too steep
			4.2	62	2.6	19	
Nov 7	04:58:40	22.4	6.8	Edge of HXIS fine FOV			45
Nov 10	08:12	20.2	1.6	1.7	9.7	1.4	15
			3.7	11	5.8	5.3	
Nov 12	02:52	25.0	2.0	1.7	11	1.9	24
			2.9	23	3.6	8.5	
Nov 12	17:04	25.0	2.7	15	4.2	6.6	15
Nov 18	14:55	23.9	1.7	1.0	13	1.3	40
			7.0	16	6.6	10	

Note: In the cases above where there are two lines per flare, the first line corresponds to the "kernel" and the second to the "tongue" seen in the HXIS images. The temperatures of the kernel and tongue were assumed to be the same.

Table 5.2.2 Energetics of the Primary Flares

Date 1980	**Apr 8**	**May 21**	**Jun 29**	**Jun 29**	**Aug 31**	**Aug 31**	**Nov 5**	**Nov 5**
HXR start time(UT)	**02:59:15**	**20:53:35**	**18:03:40**	**18:22:00**	**12:47:55**	**12:51:00**	**22:25:40**	**22:32:10**
SXR peak time (UT)	**03:07:00**	**21:05:00**	**18:04:00**	**18:25:40**	**12:49:30**	**12:52:30**	**22:28:17**	**22:35:30**
Area kernel (10^{17}cm^2)	8	22	4.8	HXIS coarse FOV	6	2	8	15
Area tongue (10^{17}cm^2)	53	40	—	—	—	—	—	35
Volume kernel (10^{26}cm^3)	6	25	1.6	(7)	3	0.8	3	14
Volume tongue (10^{26}cm^3)	62	40	—	—	—	—	—	34
HXIS Temp. (10^6K)	25	21	25	20	17	20	20	26
HXIS EM (total) (10^{48}cm^{-3})	19	103	1.7	28	3	11	3	16
$C_{max,t}/C_{max,k}$	6%	20%	—	—	—	—	—	6%
EM_k(10^{48}cm^{-3})	14	76	—	—	3	11	—	14
EM_t(10^{48}cm^{-3})	5	27	—	—	—	—	—	2
Density(kernel) (10^{10}cm^{-3})	15	17	10	(20)	10	38	10	10
Density(tongue) (10^{10}cm^{-3})	3	8	—	—	—	—	—	2
Thermal energy (kernel)(10^{29} ergs)	9	38	1.7	(12)	2	2	3	15
Thermal energy (tongue)(10^{29} ergs)	19	29	—	—	—	—	—	9
Total thermal energy (10^{29} ergs)	28	67	1.7	(12)	2	2	3	24
Energy in electrons > 25 keV(10^{29} ergs)	94	96/110	4.8	13	3	5	1.6 - 12	28
Power law index γ	4.7/6.5	3.8/3.5	3.7-7	4.7	3.3	3.3	4	3.9

Note: Filling factor assumed to be unity.

Volume and thermal energy computed assuming a density of 2×10^{11}cm^{-3} for the limb flare on 1980 June 29 at 18:25 UT.

Table 5.2.3 Parameters Calculated from Coincident Hard X-Ray and Microwave Analysis

Date 1980	Time (UT)	$\underline{T}$ (keV)	$\underline{Y}$ (10^{45} cm^{-3})	$\underline{A}_\mu$ (10^{18} cm^2)	$\underline{E}_{th}$ (10^{29} erg)	Probability[1] (%)	$\underline{f}_t$ (GHz)	$\underline{B}$ (G)	Thick target (10^{27} erg s^{-1})	Probability[2] (%)
Apr 08	03:07:06	7	20	7.3	6.7	7	6	280	25	73
May 21	20:55:54	44	2.6	3.7	9.1	~0	7.4	114	57	30
	20:56:20	40	1.9	3.4	6.6	~0	7.6	125	41	46
	20:57:30	30	1.2	3.5	4.0	~0	7.9	166	33	75
	20:58:30	32	0.5	3.4	2.7	~0	6.4	124	16	4
	21:00:30	35	0.5	3.2	2.8	~0	6.4	116	17	~0
	21:03:20	39	0.2	2.6	1.7	~0	6.3	105	7	~0
Jun 29	18:23:20	16	3.3	33	19	~0	2.0	53	23	28
Aug 31	12:48:50	48	1.4	2.9	6.1	8	8.8	127	20	0.6
Nov 05	22:26:30	33	0.5	0.1	2.3	11	—	—	6.5	28
	22:33:03	37	3.3	4.9	11	~0	13.5	262	8.2	0.1

[1] The probability of obtaining a higher value of χ^2 than that obtained for the thermal fit to the HXRBS spectrum. A probability of ~0 indicates that a value of $\chi^2 >>$ the number of degrees of freedom was obtained.

[2] The probability of obtaining a higher value of χ^2 than that obtained for the power-law fit to the HXRBS spectrum.

Table 5.2.4 Estimates of the Energies in Protons and Ions

Event			Energy in Energetic Protons and Ions (ergs)			
Date 1980	Start time (UT)	Δt (s)	Scaled estimates		Upper limits	
			>10 MeV	>0 MeV	>10 MeV	>0 MeV
May 21	20:54:32	98.3	2.0×10^{27}	1.8×10^{28}	1.1×10^{28}	1.0×10^{29}
Aug 31	21:48:31	49.2	9.3×10^{26}	8.3×10^{27}	9.3×10^{27}	8.3×10^{28}
Nov 5	22:32:40	65.5	5.7×10^{27}	5.0×10^{28}	3.1×10^{27}	2.7×10^{28}

The values listed under the column heading ">10 MeV" are upper limits on the total energy content of protons and ions with kinetic energies greater than 10 MeV. The values listed under the column heading ">0 MeV" are upper limits on the total energy content of all protons and ions included in the energetic particle spectrum. Each event is designated by its date, start time, and Δt, which specifies the duration of the impulsive phase over which the flux values were integrated.

choices, such as a power law with the low-energy cut-off as a free parameter, could change all of these values by several orders of magnitude, as the bulk of the energy is probably in protons and ions with energies <1 MeV.

5.2.3.3 Thermal Energy of the Soft X-ray Emitting Plasma

As discussed in Appendix 5B, there is considerable observational evidence that the thermal plasma emitting soft X-rays, i.e., plasma with T greater than or about 3×10^7K, is not isothermal, especially during the impulsive phase. Nevertheless, we have made estimates of the total thermal energy by assuming a single-temperature thermal source for this radiation. These estimates clearly are subject to large, systematic errors, but they should give reasonable results over restricted temperature ranges. In particular, they are expected to be more reliable at the end of the impulsive phase, when the thermal energy reaches its maximum value. At that time the plasma is closer to thermal equilibrium, and a single-temperature analysis should be more appropriate. Tables 5.2.1 and 5.2.2 show estimates of these peak thermal energies for direct comparison with the total energy in fast electrons entering a thick target during the impulsive phase.

A more comprehensive analysis technique that involves estimating the differential emission measure as a function of temperature was also used for the cases in which sufficient data were available (see Section 5.3.2). The results should give more accurate energy estimates, but again, because of the available observations and the uncertainty in the FCS calibration, they apply only in the restricted temperature range above 10^7K.

For the single temperature analysis a technique was used that is similar to the one described in Section 5.2.3.1(ii) for the thermal analysis of the hard X-ray spectrum. The single temperature analysis was carried out using the six HXIS energy bands to derive a temperature and emission measure. The same equations used for the hard X-ray analysis were also used here with the addition of estimates of the line fluxes which contribute to the counting rate in the lower energy bands.

The estimates of the source volume, required to determine the thermal energy, were obtained from the HXIS fine-field-of-view images in bands 1, 2, and 3 (3.5 to 11 keV) after the smearing effects of the instrument collimators were removed. A simple iterative technique based on the method given by Svestka *et al.* (1983) was used to deconvolve the collimator response. Unlike Svestka *et al.*, however, we continued the iterations until the χ^2 statistic stopped decreasing rather than when χ^2 became less than the number of degrees of freedom. In this way the most likely value of the source area was obtained. For the smaller sources, this was as much as a factor of 5 smaller than that which would have been obtained by the original method given by Svestka *et al.* Further details about the procedure are given by Dennis *et al.* (1984a).

In contrast to the microwave source area A_μ discussed in Section 5.2.3.1(ii), this measured source area is directly determined, but it is only the apparent area. The true area may be much smaller and may contain fine structure that was unresolved with the HXIS 8 arcsec FWHM spatial resolution. Again, we must assume some reasonable geometry to determine the source volume V_m from this measured area A_X. For most simple geometries

$$V_m \approx 0.5\ A_x^{3/2}. \qquad (5.2.13)$$

We include the filling factor ϕ such that

$$V_p = \phi\ V_m \qquad (5.2.14)$$

to allow for the possibility that the source was unresolved. Thus, we obtain the following relation for the energy in the plasma, assuming it to be isothermal:

$$E_{th}(<10^8\ K) = 4.14\times10^{-16}\ (Y\ \phi\ V_m)^{1/2}\ T\ \text{ergs}. \qquad (5.2.15)$$

(c.f. Equation 5.2.8).

In many cases, the source at the time of the peak in soft X-rays was made up of at least two separate components: a small, compact source referred to as the "kernel" by de Jager *et al.* (1983) and a more extended source with lower counting rates per pixel, referred to as the "tongue". In the present analysis, it was possible to estimate the areas of these two sources separately. Further, by assuming that their temperatures were the same, it was possible to determine their relative contribution to the total emission measure. Thus, the thermal energy in each component could be determined separately (Dennis *et al.*, 1984a). The different parameters computed for the kernel and the tongue for those flares in which they could be distinguished are listed in Tables 5.2.1 and 5.2.2.

5.2.3.4 Convective and Turbulent Motions

The BCS spectra in the Ca XIX and Fe XXV channels show a blue-shifted component and line broadening during the impulsive phase of many events. These have been interpreted as resulting from upward motions and turbulent motions, respectively (Antonucci *et al.*, 1982). The energies associated with these bulk plasma motions can be significant and have been estimated, when possible, for the prime flares studied by this group.

The most extensive analysis of bulk motions has been carried out by Antonucci *et al.* (1982, 1984). In this analysis of 25 disk flares, the observed Ca XIX spectra were fitted with a synthesized spectrum consisting of the spectrum expected from a stationary, isothermal but turbulent source plus the spectrum from an upwardly moving source with the same electron and Doppler temperatures as the stationary source. In this way, the electron and Doppler temperatures and the emission measure of the source of the principal spectrum were derived together with the flow velocity and the emission measure of the moving source.

To compute the convective and turbulent energies from these parameters, it is necessary to know the mass of the plasma involved. Antonucci *et al.* (1984) were able to derive values for the mass of the upflowing plasma by requiring that the evaporating material supply sufficient mass and energy to account for the observed coronal plasma during the thermal phase of the flare. The volume of this plasma can be inferred from the HXIS images, as already discussed in Section 5.2.2.2. Furthermore, an estimate of the cross-sectional area and separation of the loop footpoints where the chromospheric evaporation is most likely to take place can be obtained from the high energy HXIS images in energy bands 5 and 6 between 16 and 30 keV.

From the values given by Antonucci *et al.* (1984), we have computed the convective (E_{con}) and turbulent (E_{tr}) energies for three of the prime flares. These energy values are given in Table 5.2.5, with the values given by the same authors for the increase (E_{SXR}) in the total energy of the coronal plasma plus the radiative and conductive losses (E_{loss}) during the evaporation process, i.e., $E_{SXR} = E_{th} + E_{tr} + E_{loss}$.

Table 5.2.5 Parameters of the Chromospheric Evaporation

Date (1980)	Time (UT)	$\overline{n_e'}$ (10^{10} cm^{-3})	V′ (10^{26} cm^3)	$\overline{v'}$ (km s^{-1})	$v_{tr(peak)}$ (km s^{-1})	$\overline{E}_{con}$ (10^{29} ergs)	$E_{tr(peak)}$ (10^{29} ergs)	E_{SXR} (10^{29} ergs)
Apr 8	03:04	10	8	250	~90	0.4	0.05	29-39
May 21	20:53	14	24	200	~60	1.1	0.1	82-160
Nov 5	22.36	13	11	200	~60	0.5	0.04	27-47

The two remaining prime flares not analysed by Antonucci *et al.* (1984), i.e., 1980 August 31 and June 29, showed very little blue shift or asymmetric line broadening. The 1980 June 29 flare occurred on the limb, and such flares typically do not have blue-shifted components or asymmetrically broadened X-ray line profiles during the impulsive phase. Presumably this is because the line of sight of the instrument is perpendicular to the direction of motion of the bulk of the moving plasma. However, symmetrical line broadening in excess of what would be expected from purely thermal motions is observed for limb flares, especially during the impulsive phase. The 1980 August 31 double flare was a compact event, which showed very little asymmetric broadening during either flare (Strong *et al.*, 1984).

The procedure to determine the turbulent energy from the symmetrical line broadening was similar to that described above. Spectral fits were obtained over the full wavelength range in the BCS Ca XVII-XIX and Fe XXIV-XXV channels. A synthetic spectrum was computed by assuming an isothermal model, and a best fit to the data was obtained which minimized the χ^2 parameter by varying the electron temperature, total line width, and emission measure. The excess line broadening was determined by subtracting the instrumental width and the contribution due to thermal motions (assuming that the ion and electron temperatures were equal). For the 1980 June 29 flare, the effect of the X-ray source size in the East-West direction (0.75 arc min) was included. The excess line broadening can be expressed as an ionic velocity. The values of this parameter obtained from the calcium and iron observations were found to be in good agreement with one another, giving confidence in the instrumental calibrations and justification for the isothermal assumption used in determining the excess line width.

The resultant turbulent energies are shown in Figure 5.3.8 and 5.3.9 for the two flares under consideration. The mass of the plasma was determined from a multi-thermal analysis for the emission measure, assuming that the volume remained constant throughout the flare. A filling factor of unity was used, and the volumes were assumed to remain constant equal to the values derived from the HXIS images given in Table 5.2.3. Since the mass was determined from a multi-thermal emission measure model for temperatures above 10^7K, the calculated turbulent energies are appropriate for the high temperature component only. The results are summarized in Table 5.2.6. The turbulent energies are a factor of 20 to 100 less than the energies in fast electrons above 25 keV computed assuming thick-target interactions.

Table 5.2.6 Turbulent Energies

Date (1980)	Time (UT)	E_{tr}(peak) (erg)	Assumed volume (cm^3)
31 Aug	12:43:54	1.3×10^{28}	3×10^{26}
31 Aug	12:51:54	5.6×10^{27}	8 x 10^{25}
29 Jun	18:23:16	3.5×10^{28}	7 x 10^{25}

5.2.3.5 Radiant Energy in Hα

An estimate of the radiant energy in Hα during the impulsive phase of the second flare on 1980 November 5 was made on the basis of spectra taken with the multi-slit spectrograph operated at the San Fernando Observatory. No useful spectra were obtained until the instrument was triggered into the flare mode at 22:34:21 UT, the beginning of the second hard X-ray maximum of the second flare (see Figure 5A.12). After that time one spectrum was recorded on 35 mm film every 2 s with the slits stepping 2.6 arcsec between exposures. The extremities of the flare kernels at the flare maximum were approximately 31 arc sec apart in the direction of slit motion. Consequently, with the 51 arc sec slit spacing, the flare kernels were sampled in groups of 12 consecutive spectra with intervening intervals of 20 arc sec when the slits were not positioned on any bright part of the flare. The total radiant Hα intensity, ΔI, in excess of the quiet Sun was obtained from the photographically recorded spectra by using the relative continuum intensity given in the Photometric Atlas of the Solar Spectrum (Minnert *et al.*, 1940) and the Labs and Neckel (1968, 1970) absolute calibrations. The three series of spectra obtained before the end of the impulsive phase gave nearly the same value for ΔI: 1.5 x 10^8 ergs s^{-1} sr^{-1}.

The total energy radiated in Hα can be determined from the measured intensities and the area $\underline{A}$ of the flare kernel of < 100 (arc sec)^2, determined from the HeI D_3 filtergrams (see Appendix 5A). The average power $\underline{P}$ radiated in Hα during the second peak of the flare was computed from the relation (Canfield *et al.*, 1980):

$$\underline{P} = 2\pi\Delta I\ \underline{A} = 4.9\ x\ 10^{26}\ \text{ergs s}^{-1}.$$

Since the second peak lasted for ~ 120 s and contained only about a quarter of the total number of hard X-rays detected with HXRBS during the flare, our best estimate for the total Hα radiated energy during the impulsive phase of the flare is 4($\underline{P}$ × 120 s) = 2.3 × 10^{29} ergs.

5.2.4 The 1980 April 8 Flare

The April 8 flare is unique among the set studied by us in that it was observed with the P78-1 satellite as well as with SMM. We have therefore chosen this event to illustrate the various approaches that we pursued in our investigation of flare energetics. Observations of hard X-ray spectra were obtained with HXRBS, images and X-ray spectra were obtained with HXIS, soft X-ray spectra were obtained with BCS, and images in the principal FCS set of lines were obtained throughout this event. UVSP observations produced a series of images in the density-sensitive lines of Si IV and O IV before the onset of the impulsive phase. The P78-1 observations include soft X-ray spectra, from which we selected the O VII, Ca XIX, and Fe XXV lines for analysis.

In Figure 5.2.1 we show the radiated energy in hard X-rays as a function of time for this flare as determined from power-law fits to the HXRBS spectral data. The power-law spectral index γ is plotted as a function of time in Figure 5.2.2, together with the power flux of electrons above 30 keV entering a thick target as derived from the power-law fits. Figure 5.2.3 shows the energy in electrons above 25 keV integrated from the start of the flare for comparison with the thermal energy in the soft X-ray emitting plasma. Two estimates of the thermal energy are plotted. The one marked "HXIS (single temp)" was obtained from isothermal fits to the HXIS data as described in Section 5.2.3.3. The source density was assumed to be 10^{10} cm^{-3} to obtain the plotted energy from the temperature and emission measure resulting from the fitting procedure. The points marked "BCS and HXIS" were obtained from a full differential emission measure (DEM) analysis with both BCS and HXIS data. The DEM distribution was integrated over temperatures from 10^7 to 5 × 10^7K, and the source volumes obtained from HXIS images were used to compute the total thermal energies plotted.

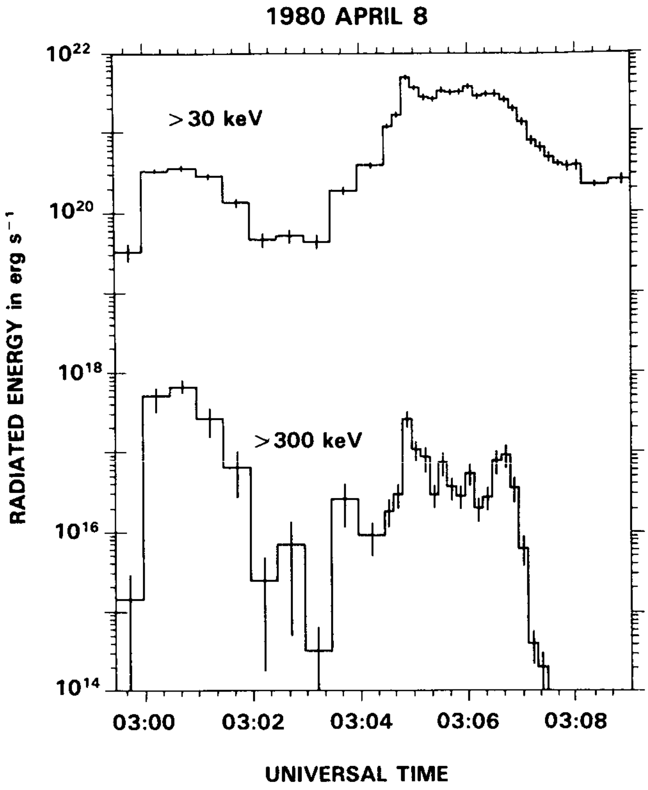

Figure 5.2.1 Radiated energy in hard X-rays for the 1980 April 8 flare. The vertical error bars represent ± 1σ uncertainties based on the HXRBS counts; the horizontal bars represent the time interval of the observations.

The effect of different assumptions about the temperature distribution and the densities or volumes can be seen by comparison of the two curves shown in Figure 5.2.3 for the thermal energy. If we force the single-temperature model to agree with the multi-thermal analysis at the end of the impulsive phase, say at 03:08 UT, by adjusting the assumed density, then the multi-thermal analysis gives about an order of magnitude more energy near the start of the impulsive phase, say at 03:04 UT. This is presumably because of a lower-temperature component with T near 10^7K that does not give a significant contribution in the HXIS energy range, at least not so that the single temperature analysis can reveal its presence. This result suggests significant preheating before the appearance of hard X-rays for this particular flare.

Figure 5.2.4 shows the results of the analysis of the hard X-ray data, assuming that the source was thermal and that the electron spectrum could be represented with a single effective temperature. The effective temperature and emission measure are plotted as a function of time, as obtained from least-squares fits to the HXRBS data. The total energy of the plasma is also plotted as a function of time, assuming a source density of 10^9 cm^{-3}.

The density determinations made possible with observations of the helium-like lines of O VII, obtained with the P78-1 satellite, enable us to obtain an estimate of the density and hence the volume of the soft X-ray emitting source at ~ 2 × 10^6K (Doschek *et al.*, 1981), and these are plotted as a function of time in Figures 5.2.5 and 5.2.6. During the impulsive phase of the flare, the density and hence the volume derived from the P78-1 observations are uncertain by as much as an order of magnitude, but after the peak in the density

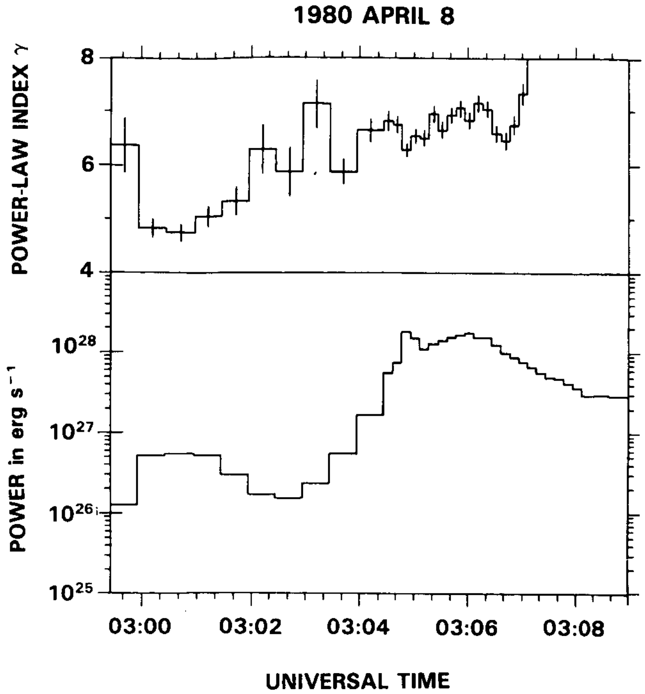

Figure 5.2.2 Power flux of electrons above 30 keV into a thick target computed from the HXRBS data for the 1980 April 8 flare. The top plot shows the HXRBS power-law spectral index on the same time scale.

estimate at approximately 03:05 UT, the uncertainties are less than a factor of 3.

In addition to the satellite observations, records of microwave emissions from the the same flare are available from the Toyokawa Observatory (courtesy of S. Enome). Under the assumptions indicated in Section 5.2.3.1(ii), coincident analysis of the hard X-ray and microwave observations gives the area and hence an estimate of the apparent source volume associated with the most energetic electrons. These volume estimates, plotted as a function of time, together with those obtained from HXIS images at 3.5 to 11.5 keV are also shown in Figure 5.2.6. These observations show that the estimated volume of the 2×10^6K plasma is 3 orders of magnitude less than the apparent volume of the hard X-ray source throughout the impulsive phase of the flare, but it increases monotonically until the two volumes are comparable at the end of the flare. Throughout the impulsive phase, the apparent volume estimated from coincident analysis of HXRBS and Toyokawa observations is comparable to the volume of the "tongue" source observed with HXIS.

The density of the hard X-ray and microwave source can be estimated from the apparent volume and the hard X-ray emission measure. This density parameter, shown in Figure 5.2.5, is seen to be relatively constant throughout the event and of the order of 10^9 cm^{-3}, justifying the use of this value in computing the thermal plasma energy plotted in Figure 5.2.4.

The parameters characterizing the chromospheric evaporation for the 1980 April 8 flare are plotted versus time in Figure 5.2.7. The plotted parameters were determined from spectral fits to Ca XIX spectra determined with BCS as described in Section 5.2.3.4. The corresponding total energies are given in Table 5.2.5.

5.2.5 Discussion

We have computed the impulsive phase energies in various components of the prime flares selected by this group and the main results are summarized in Table 5.2.7.

The total energy in fast electrons during the impulsive phase and the thermal energy in the soft X-ray emitting plasma at the end of the impulsive phase are the two most important components of these flares from an energetics standpoint. If the hard X-rays are produced by thick-target interactions of the fast electrons, the total energy in electrons above 25 keV is almost embarassingly large compared with the energy of the soft-X-ray-emitting plasma. If the lower-energy cut-off is dropped to 10 keV, as appears reasonable, at least for the early part of the impulsive phase of some flares, then the calculated energy in fast electrons becomes even higher. A plot of the thermal energy of the soft-X-ray-emitting plasma against the energy in electrons above 25 keV, $\underline{W}(>25$ keV), is shown in Figure 5.2.8. A strong correlation with a coefficient of 0.8 is found between these two quantities. Although this correlation is considerably better than that expected from the Big Flare Syndrome (Kahler 1982), correlations calculated for different models show similarly high correlation coefficients (see Section 5.4.2). There are other serious problems with this correlation, so that it cannot be used to argue in favor of thick-target interactions or of a causal relation between the fast electrons and the thermal plasma. These problems are discussed briefly here.

(1) The low-energy cut-off in the electron spectrum is unknown and may be different for different flares. This can cause order-of-magnitude errors in the estimates of the total energy in fast electrons.

(2) The filling factor for the thermal plasma is unknown and may be different for different flares. Introduction of a fractional filling factor will decrease the thermal energy by $\phi^{1/2}$. It has been argued that ϕ was as small as 10^{-2} during the flare on 1980 April 30 (de Jager *et al.*, 1983), 3×10^{-3} to 3×10^{-2} during the flare on 1980 November 5 (Wolfson *et al.*, 1983), and 10^{-4} for the same flare (Martens *et al.*, 1984). Filling factors this small would decrease the thermal energy by one or two orders of magnitude, thus destroying the similarity with the energy in fast electrons.

(3) The hard X-ray spectral fits may be contaminated by the high-energy tail of the thermal distribution, particu-

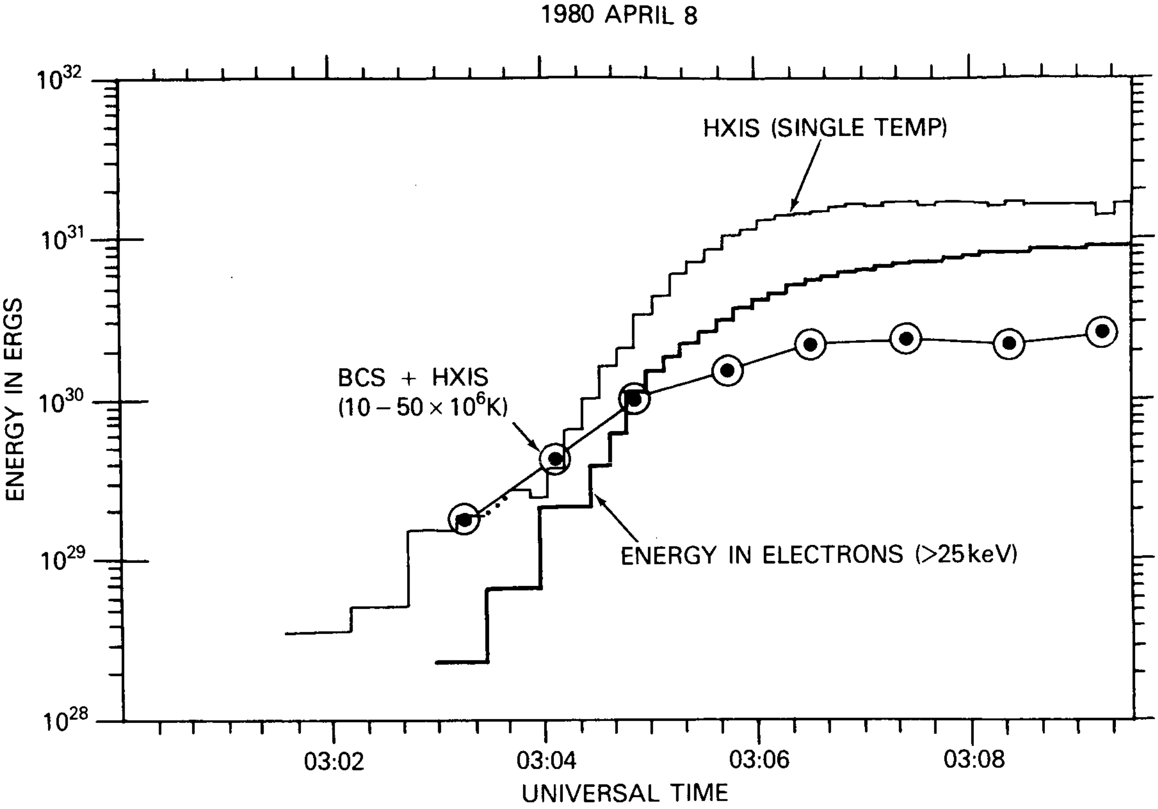

Figure 5.2.3 Energy in > 25 keV electrons and in the soft-X-ray-emitting thermal plasma as a function of time for the impulsive phase of the 1980 April 8 flare. The energy in electrons above 25 keV was computed from power-law fits to the HXRBS data assuming thick-target interactions. The energy in the soft-X-ray-emitting plasma was computed in two ways. In one case marked "HXIS (single temp)", a single temperature thermal spectrum was fitted to the HXIS spectral data by using the results of the HXIS count rate prediction program. In the other case, a full multi-temperature DEM analysis was carried out using BCS and HXIS data for temperatures from 10^7 to 5 × 10^7K.

larly toward the end of the impulsive phase when the soft X-ray flux is very large, and the high temperature component (3 × 10^7K) detected by Lin *et al.* (1981) is expected to dominate. Also, when the X-ray spectrum becomes steeper than, say, ϵ^{-6} or ϵ^{-7}, the relatively poor energy resolution of scintillation counters makes it impossible to determine the true spectrum with any accuracy. As a consequence of these two factors, the energy in fast electrons may have been overestimated in some cases.

(4) Not all of the hard X-rays may have been produced in thick-target electron interactions. A considerable fraction of the total X-ray flux may be produced from a thermal source, particularly in the later stages of the impulsive phase when footpoints can no longer be resolved in the hard X-ray images. If the X-rays are mainly from a thermal distribution of electrons, then a value of $\sim 2 \times 10^{10}$ cm^{-3} for the unknown density will make the energy in such a thermal source equal to the energy calculated assuming thick-target interactions (Smith and Lilliquist, 1979). With the thermal model described in Section 5.2.3.1 (ii) in which the hard X-rays and microwaves are assumed to come from a common source, the density and energy content of the energetic electrons are uniquely specified by the observed emissions. The total energy integrated over the whole flare, however, depends on the rate of energy input to the electrons and on unspecified loss mechanisms. It is, therefore, not known if the energetic electrons could supply the thermal energy of the plasma at temperatures greater than or about 10^7 K. Smith (1985) suggests that only 10% or less of the hard X-rays are produced in thick-target interactions, mostly in the first 1 or 2 min of the impulsive phase. He postulates that the energy release mechanism puts most of the energy into heating after that time. Rust (1984) also argues that only a small fraction of the observed chromospheric evaporation is produced by electron beams and that such

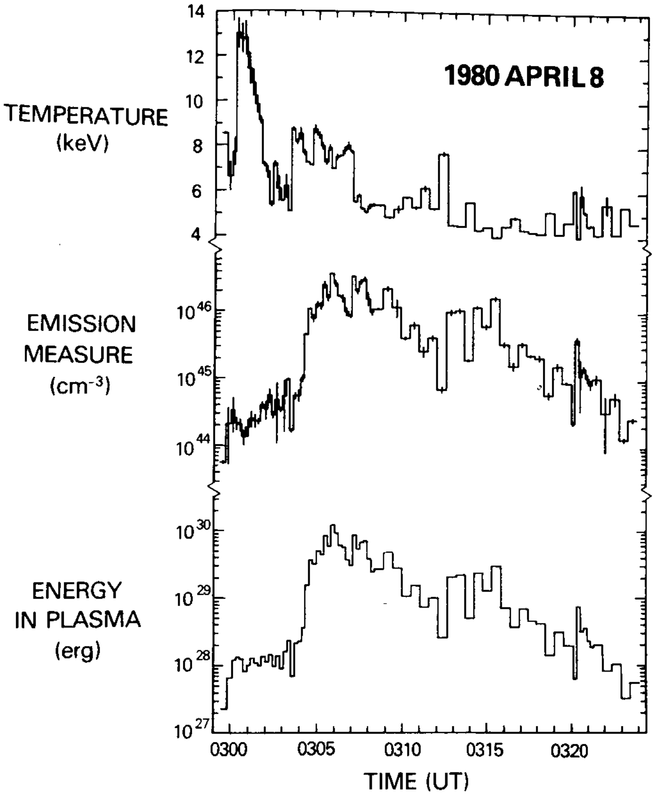

Figure 5.2.4 Temperature and emission measure as a function of time for the 1980 April 8 flare computed from HXRBS data between 27 and 467 keV using a single-temperature parameterization of the hard X-ray spectra. The total energy of the plasma is also plotted for a constant source density of 10^9 cm^{-3}.

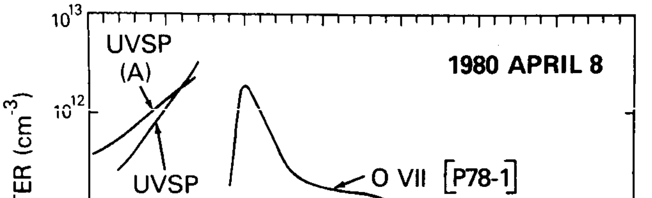

Figure 5.2.5 Source density as a function of time for the 1980 April 8 flare.

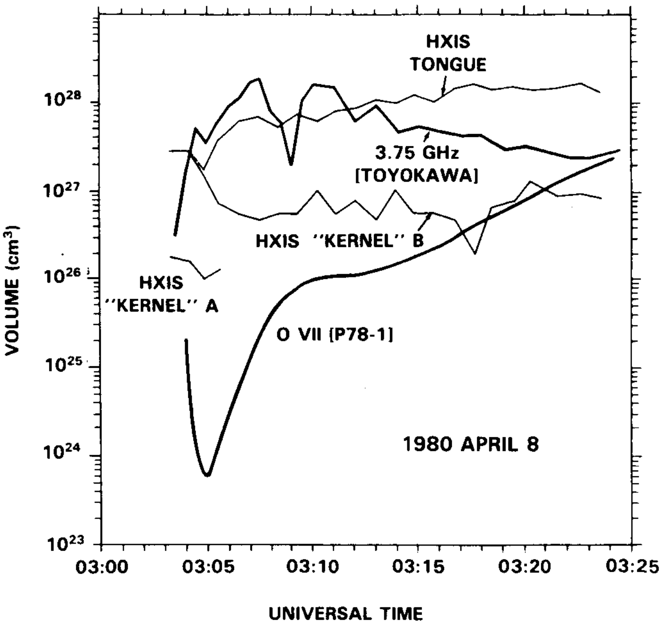

Figure 5.2.6 Source volumes for the 1980 April 8 flare determined from the HXIS soft X-ray images, the P78-1 density-sensitive line data, and the hard X-ray/microwave analysis discussed in the text.

beams are energetically unimportant when compared to conduction.

In addition to the total energies of the impulsive phase, we have determined the energies as a function of time for some flares. Figure 5.2.3 is a plot of the different components of the flare energy as a function of time for the impulsive phase of the 1980 April 8 flare; Figure 5.2.9 is a similar plot for the 1980 May 21 flare, from Antonucci *et al.* (1984). In both cases, the build-up in thermal energy of the soft X-ray emitting plasma is consistent with the depostion of energy into a thick target by fast electrons.

For the May 21 flare, when the impulsive phase was relatively long, lasting for about 10 min until ~21:05 UT, the radiation losses are significant. Depending on the assumed volume, the thermal energy is between 1 and 6 times larger than the accumulated radiation losses at 21:05 UT. For the other flares with shorter impulsive phases, the radiative losses tend to be less important, as can be seen from a comparison of $\underline{E}_{th}(>10^7K)$ and $\underline{E}_{SXR}$ in Table 5.2.7.

5.2.6 Conclusion

It is clear that with the present state of the observations, the study of flare energetics during the impulsive phase is a very poor way of discriminating between different flare models. Ideally, it would be possible to determine the fraction of the total energy that goes into accelerating electrons versus the fraction directly heating the plasma. We are clearly a long way from being able to make that differentiation,

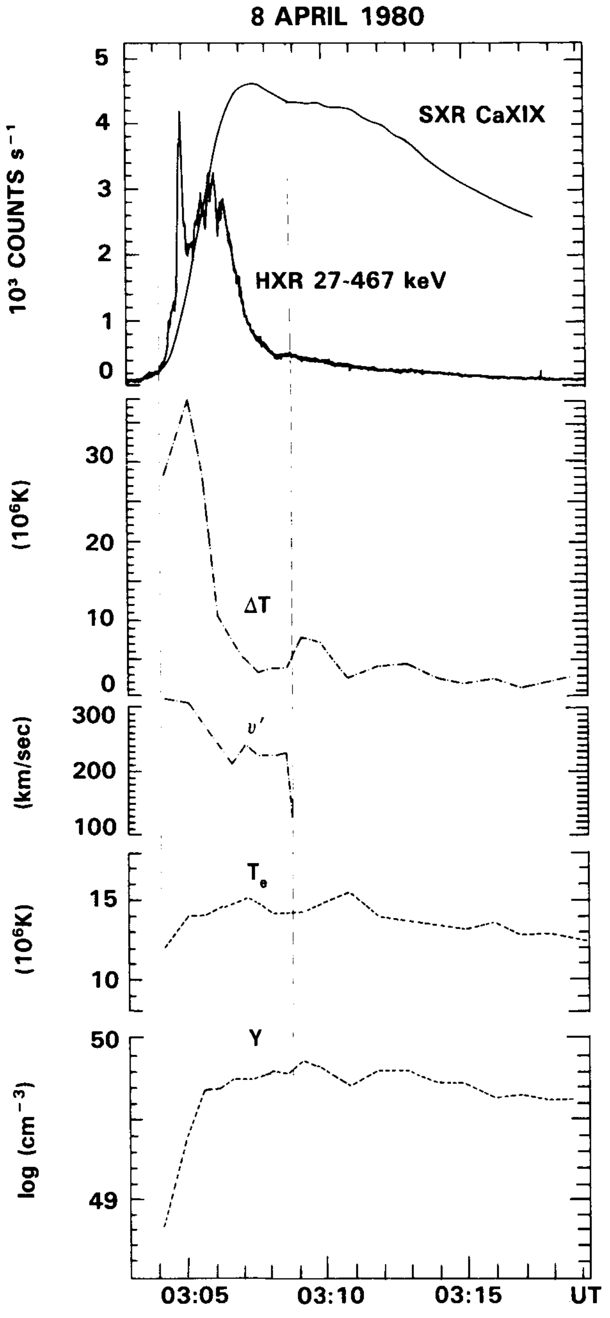

Figure 5.2.7 The time variation of the parameters characterizing the chromospheric evaporation for the 1980 April 8 flare. The following derived quantities are plotted as a function of time with the Ca XIX and hard X-ray rates shown for reference: the temperature difference ΔT between the ion and the electron temperatures, the upward component of the velocity v′, the electron temperature T_e, and the Ca XIX emission measure Y (from Antonucci *et al.,* 1984.). Note that the plotted difference, ΔT, between the Doppler and electron temperature is a measure of the non-thermal line broadening attributed to plasma turbulence.

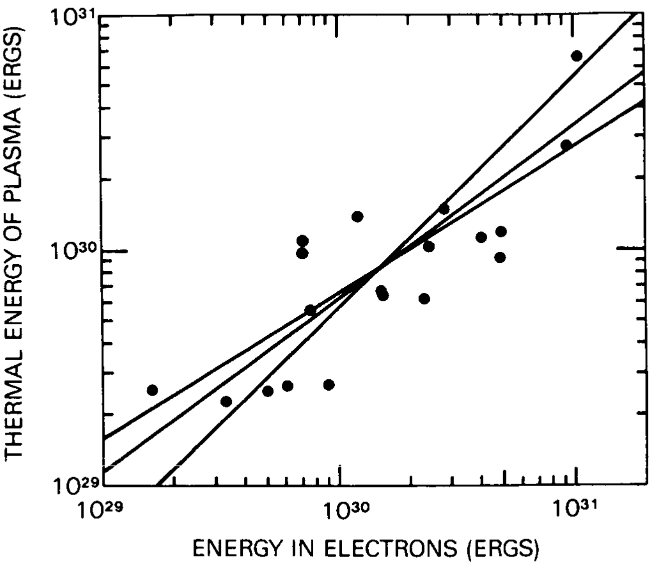

Figure 5.2.8 Plot of the thermal energy U at the time of the peak soft X-ray flux versus the energy in electrons W (> 25 KeV) entering a thick target integrated up to the same time. Each point corresponds to one of the 19 flares listed in Table 1, for which there is an estimate of U based on HXIS observations. Note that the plotted value for U is the sum of the energies in the "tongue" and "kernel" sources seen in the HXIS images.

although the data, particularly the hard X-ray imaging observations, suggest that some significant fraction of the energy does go to accelerate electrons to energies above 20 keV.

To improve this situation, future observations must address the fundamental constraints which have limited our analysis. The most important of these is the resolution of the thermal or non-thermal character of the hard X-ray source. It is not clear at present how this will be achieved, although hard X-ray imaging to higher energies and with better spatial and temporal resolution will be important. Also, measurements of the hard X-ray spectrum with higher spectral resolution than is possible with scintillation counters will allow spectra steeper than ϵ^{-7} to be determined and will also enable X-rays from plasma with temperatures up to 3 × 10^7K to be separated more clearly from the higher-energy component. Moreover, by combining observations with improved spectral and spatial resolution, the spectrum of accelerated electrons below 20-30 keV can be determined, so that a better estimate of the total energy in these electrons can be made.

As far as improvements in the estimates of the energy in the soft-X-ray emitting plasma is concerned, it is clear that better estimates of the emission from plasma at temperatures below 10^7K must be made and that the filling factor must be determined at all energies. A wide range of temper-

Table 5.2.7 Summary of Flare Energies (in units of 10^{29} ergs)

Date 1980	Time (UT)	W(>25 keV)	$E_{th}(>10^8K)$	$E_{th}(>10^7K)$	E_{SXR}	E_{tr}	E(Hα)
Apr 8	03:07	94	7	28	29-39	—	—
May 21	21:05	96/100	9	67	82-160	—	—
Jun 29	18:04	5	—	1.7	—	—	—
	18:26	13	19	12	—	3.5	—
Aug 31	12:49:30	3	6	2	—	1.3	—
	12:52:30	5	—	2	—	0.56	—
Nov 5	22:28:17	1.6-12	0.23	3	—	—	—
	22:35:30	28	11	24	27-47	—	2.3

W(>25 keV), total energy in electrons above 25 keV calculated from the hard X-ray spectra assuming thick-target interactions; $E_{th}(>10^8K)$, thermal energy at the time of the peak hard X-ray flux calculated from the hard X-ray spectrum assuming a source with a temperature of $>10^8K$; $E_{th}(>10^7K)$, thermal energy at the time of the peak soft X-ray flux computed from a multi-thermal analysis with $10^7 < T < 5 \times 10^7K$ and the HXIS source area; E_{SXR}, the increase in the thermal and turbulent energy of the plasma plus the total radiated and conducted energy losses up until the time of the peak in soft X-rays (see text); E_{tr}(peak), peak energy of the turbulent plasma motions; E(Hα), radiant energy in Hα integrated over the duration of the impulsive phase.

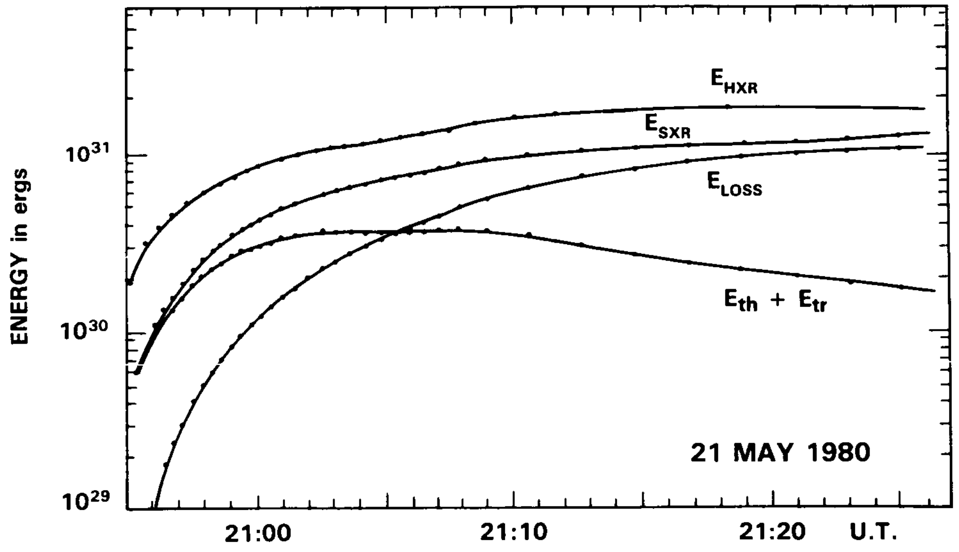

Figure 5.2.9 Temporal evolution of the following quantities during the 1980 May 21 flare from Antonucci *et al.* (1984): E_{HXR}, the total energy input to the chromosphere by non-thermal electrons above 25 keV from the flare onset time t_o up to the time t plotted; E_{SXR}, the total energy input to the soft X-ray emitting plasma; E_{th}, the thermal energy of the coronal plasma at time t; E_{tr}, the turbulent energy of the coronal plasma at time t; E_{loss}, the integral of the radiation and conductive loss rates from t_o to t. Note that $E_{SXR} = E_{th} + E_{tr} + E_{loss}$. The quantities derived from the soft X-ray emission were calculated assuming a lower limit volume of 2.4×10^{27} cm^3.

atures is involved during the impulsive phase, and single temperature analysis is inadequate, given the improvements in the observations. Multi-thermal analysis techniques, however, are limited in the detail with which the temperature distribution can be determined, even with more accurate observations.

5.3 THE ENERGETICS OF THE GRADUAL PHASE

K.T. Strong, R.D. Bentley, P.L. Bornmann, M.E. Bruner, P.J. Cargill, J.G. Doyle, J.R. Lemen, R. Pallavicini, G. Peres, S. Serio, G.M. Simnett, J. Sylwester, and N.J. Veck

5.3.1 Introduction

The gradual phase of a flare is best characterized by the smooth rise and decay of the soft X-rays (see Figure 5A.2). Just from inspection of the soft X-ray light curves of some typical flares, it is evident that the gradual phase comprises several different stages. During the rise of the X-ray emission, a completely different energy budget from that of the decay will be produced. Many flares show multiple peaks in their light curves, indicating that energy is released after the initial burst. The location of any such secondary energy release will also profoundly affect the relative importance of the terms in the energy budget of the flare.

The soft X-ray emission produced by the higher-temperature ($> 10^7$ K) plasma rises and decays more rapidly and peaks earlier than that produced by the cooler plasma (10^6 - 10^7 K). The impulsive phase usually occurs during the rise of the soft X-ray emission but there is no clear evidence of an impulsive component in the soft X-ray signal. Hence, in an energetics study the important question arises of what, if any, is the link between the impulsive and gradual phases.

We have avoided using the term "thermal phase" because it is misleading; a number of non-thermal energetics terms are associated with the gradual phase. The mass motions are an example; it is not clear whether they are peculiar to the early stages of a flare or whether they are also present later in the flare, which seems to be likely, as mass motions have been detected even in quiescent active regions (Acton *et al.*, 1981). We therefore attempted to evaluate the non-thermal terms as well as the thermal energy throughout the gradual phase of the five prime flares.

As the flare observations made with SMM were not specifically designed to address the energetics problem, our choice of flares (see Appendix 5A) represents a compromise. We identified a number of different "types" of flares that, although sharing the same physical processes, had somewhat different physical characteristics.

The Skylab Solar Flares Workshop (Sturrock 1980a) laid the foundations for the methodology used in this section, and we compare our results with those in the chapter by Moore *et al.* (1980), who reached five main conclusions about the gradual phase:

- the typical density of the soft X-ray emitting plasma is between 10^{11} and 10^{12} cm^{-3} for compact flares and between 10^{10} and 10^{11} cm^{-3} for a large-area flare;
- cooling is by conduction and radiation in roughly equal proportions;
- continual heating is needed in the decay phase of two-ribbon flares;
- continual heating is probably not needed in compact events;
- most of the soft-X-ray-emitting plasma results from "chromospheric evaporation".

Our goal was to reexamine these problems with the data from SMM and other supporting instruments as well as to take advantage of recent theoretical advances. SMM is capable of measuring coronal temperatures more accurately and with a better cadence than has been possible before. The SMM data set is also unique in that the complete transit of an active region was observed, with soft X-ray and UV images being taken every few minutes. We are therefore able to establish the pre-flare conditions of the region and see whether anything has changed as a result of the flare.

In the next subsection we describe the assumptions made in attempting to determine the required plasma parameters. The derived parameters for the five prime flares are presented, and the role of numerical simulations is discussed. Finally, we consider the overall implications of our results and discuss how both theory and observations have evolved since the Skylab workshop.

5.3.2 The Basic Physical Expressions

The quantities needed for this study are defined in terms of the fundamental plasma parameters of electron temperature (T_e), electron density (N_e), plasma volume (V), plasma velocity (v), and height (h). The four basic energies that we wish to obtain throughout the flares are the thermal energy (E_{th}) of the plasma,

$$E_{th} = 3\ N_e\ k\ T_e\ V \text{ ergs}; \qquad (5.3.1)$$

the kinetic energy (E_k) of the plasma,

$$E_k = 1/2\ M_p\ N_e\ V\ v^2 \text{ ergs}; \qquad (5.3.2)$$

the potential energy (E_p) of the coronal plasma,

$$E_p = M_p\ N_e\ V\ g_o\ h \text{ ergs} \qquad (5.3.3)$$

(where M_p is the proton mass and g_o is the gravitational acceleration at the solar surface); and the stored ionization energy in the plasma (E_i), which is the sum of the ioniza-